Journal of the Mechanics and Physics of Solids 62 (2014) 163–180

Contents lists available at ScienceDirect

Journal of the Mechanics and Physics of Solids

journal homepage: www.elsevier.com/locate/jmps

Spatial resolution of wrinkle patterns in thin elastic sheets at finite strain

Michael Taylor [a], Katia Bertoldi [a,c,*], David J. Steigmann [b]

[a] School of Engineering and Applied Sciences, Harvard University, Cambridge, MA, United States
[b] Department of Mechanical Engineering, University of California, Berkeley, CA, United States
[c] Kavli Institute for Bionano Science and Technology, Harvard University, Cambridge, MA, United States

ARTICLE INFO

Article history:
Received 26 March 2013
Received in revised form
19 August 2013
Accepted 27 September 2013
Available online 16 October 2013

Keywords:
Wrinkling
Nonlinear elasticity
Thin elastic sheets

ABSTRACT

Koiter's nonlinear plate theory is used to simulate the wrinkling patterns observed in stretched thin elastic sheets. The phenomenon considered is associated with wrinkle patterns distributed over the interior of the sheet, in regions where the stretching and bending energies are of the same order of magnitude. Numerical solutions to several equilibrium boundary-value problems are obtained by the method of dynamic relaxation based on a dissipative dynamical system and compared with existing experimental, numerical, and analytical results.

1. Introduction

Thin elastic sheets develop surface undulations, or wrinkles, in the presence of small compressive stress. The study of this phenomenon has its roots in the pioneering works by Wagner (1929) and Reissner (1938). In recent years, interest in thin sheets has greatly increased due to their relevance in a wide array of applications such as biological tissues (Ben Amar and Dervaux, 2008), integrated circuits (Kim et al., 2008), and solar sails (Vulpetti et al., 2008; Taylor and Steigmann, 2009; Kezerashvili, 2010). As a result, wrinkling has recently attracted considerable attention among engineers (Healey et al., 2013; Wong and Pellegrino, 2006a–c; Pipkin, 1986; Steigmann, 1990; Zheng, 2009), physicists (Davidovitch et al., 2011; Cerda and Mahadevan, 2003; Vandeparre et al., 2011) and biologists (Kareklas et al., 2013).

The problem may be regarded as one of characterizing the deformation of a sheet well into the post-buckling range, though it differs from conventional buckling in that it is attended by significant stretching. To model details of the wrinkle patterns such as wavelength and amplitude, an appropriate theory must account for the flexural stiffness of the sheet. This effectively introduces a local length scale in the theory, which in turn figures in the wavelengths of the wrinkles.

Typical approaches to characterizing the wrinkled regions in thin sheets in recent years can be placed into three general categories: tension-field theory, analytical approaches based on a Föppl–von Kármán framework and finite element simulations based on buckling analyses.

Tension-field theory was devised (Pipkin, 1986; Steigmann, 1990; Haseganu and Steigmann, 1994) to circumvent the rather formidable challenges associated with developing nonlinear models incorporating a local length scale. There, the bending stiffness is ignored and the wrinkles are regarded as being continuously distributed over interior portions of the

* Corresponding author at: School of Engineering and Applied Sciences, Harvard University, Cambridge, MA, United States. Tel.: +1 857 234 7352.
E-mail address: bertoldi@seas.harvard.edu (K. Bertoldi).

0022-5096/$ - see front matter © 2013 Elsevier Ltd. All rights reserved.
http://dx.doi.org/10.1016/j.jmps.2013.09.024

sheet—regions which must be determined in the course of solving the associated boundary-value problem. Tension-field theory has been rigorously established in recent years (Pipkin, 1986; LeDret and Raoult, 1995) as the appropriate leading-order model as sheet thickness tends to zero. It is also far more tractable than models which incorporate flexural stiffness, but offers no information about the details of the wrinkle patterns. At best, it is useful for assessing the stress distribution in sheets which are so thin that the compressive buckling stress is negligible in comparison to the tensile stress transmitted along the wrinkle trajectories.

Alternatively, other analytical approaches are based on minimizing an energy functional that incorporates both membrane and bending contributions. These are usually based on a geometrically nonlinear Föppl–von Kármán framework augmented by a constraint leading to relationships for the amplitude and wavelength of wrinkles in a specific problem of interest (Cerda et al., 2002; Cerda and Mahadevan, 2003; Efimenko et al., 2005; Wong and Pellegrino, 2006b; Vandeparre et al., 2010; Puntel et al., 2011; Davidovitch et al., 2011; Vandeparre et al., 2011; Schroll et al., 2011). However, it has been shown via the method of gamma-convergence that the Föppl–von Kármán equations can be rigorously derived from three-dimensional elasticity theory only if the deformation of the midplane is isometric (Friesecke et al., 2006).

Finally, numerical analyses via the finite element method have been used to study wrinkling in thin sheets (Wong and Pellegrino, 2006c; Zheng, 2009; Nayyar et al., 2011). Here, the sheet is discretized using shell elements. First the buckling modes are determined by an eigenvalue analysis. A certain number of mode shapes are then used as an imperfection in a post-buckling analysis to determine the equilibrium state of the sheet. The wrinkling pattern has been found to be significantly affected by the shell formulation used in the simulations and the determination of the shell element which best characterizes the wrinkled regions remains open (Wong and Pellegrino, 2006c; Zheng, 2009). In a notable recent work by Healey et al. (2013), a more complete bifurcation analysis is carried out on a hyperelastic sheet under tension using a conformal finite element discretization and Euler–Newton arc-length continuation based upon a modification of the Föppl–von Kármán model.

The goal of the present paper is to provide an accurate model of thin sheets which may be used to predict the details of the deformation in wrinkled regions for general problems, and to illustrate its use through the numerical solution of several equilibrium problems in which wrinkling figures prominently. The analysis is based on a model recently derived from three-dimensional nonlinear elasticity which effectively extends Koiter's theory (Koiter, 1960, 1966) to deformations that involve significant stretching (Steigmann, 2013). The theory is successfully implemented within a finite difference framework and used to solve a variety of problems involving wrinkling. The simulations show excellent agreement with experimental results available in the literature and demonstrate that the proposed framework is robust and can be effectively used to investigate the behavior of thin sheets.

The basic model is discussed in Steigmann (2010, 2013), and its relationship to three-dimensional elasticity theory is summarized in Section 2. In Section 3, the equilibrium equations of the theory are replaced by an artificial dissipative dynamical system for the purpose of effecting a solution procedure based on the method of dynamic relaxation (Silling, 1988, 1989). This is discretized using a spatial finite difference mesh derived from Green's theorem, together with explicit finite differencing in (artificial) time. Equilibria of this system are precisely the solutions to the original physical system, and are recovered by advancing the dynamical solution until the transient response has run its course. Several examples highlighting wrinkle formation are discussed in Section 4. In the first example, we present a simulation of the uniaxial tension of a rectangular silicone rubber sheet inspired by numerous studies (Cerda and Mahadevan, 2003; Zheng, 2009; Puntel et al., 2011; Nayyar et al., 2011; Healey et al., 2013). Equilibrium deformations and wrinkle properties found using the present model are compared with the corresponding experimental and finite element results of Zheng (2009) over a range of applied displacement. For the next example, we simulate wrinkling induced by the in-plane shearing of a rectangular Kapton sheet based on experiments by Wong and Pellegrino (2006a). We compare our results with the experimental data for two applied shearing displacements. In the final two examples we focus on thin sheets with central holes and compare results from the present model with those from tension-field theory. In the penultimate example, we simulate the uniaxial tension of a rectangular Kapton sheet with an unloaded central hole. Finally, we conduct a simulation of the combined twist and pull-up of a central hub in an annular sheet. The results from these four examples not only show excellent agreement with available experimental data, but also support a conjecture offered in Steigmann (1990) to the effect that the stress delivered by tension-field theory furnishes a reliable estimate despite the inability of that theory to model the deformation in wrinkled regions.

2. Finite strain model for thin elastic sheets

In this section we summarize relevant aspects of the model and specialize it to the case of isotropic materials. This model will then serve a basis of the numerical analysis that is the focus of this study.

2.1. Summary of notation

To describe the theory, standard notation is used throughout. Bold face is used for vectors and tensors and indices to denote their components. Latin indices take values in $\{1,2,3\}$; Greek in $\{1,2\}$. The latter are associated with in-plane coordinates and associated vector and tensor components. A dot between bold symbols is used to denote the standard inner product. Thus, if $\mathbf{A}_1$ and $\mathbf{A}_2$ are second-order tensors, then $\mathbf{A}_1 \cdot \mathbf{A}_2 = \mathrm{tr}(\mathbf{A}_1\mathbf{A}_2^t)$, where $\mathrm{tr}(\cdot)$ is the trace and the superscript t is

used to denote the transpose. The norm of a tensor $\mathbf{A}$ is $|\mathbf{A}| = \sqrt{\mathbf{A}\cdot\mathbf{A}}$. The linear operator Sym(·) delivers the symmetric part of its second-order tensor argument; the notation $\otimes$ identifies the standard tensor product of vectors. If $\mathcal{C}$ is a fourth-order tensor, then $\mathcal{C}[\mathbf{A}]$ is the second-order tensor with Cartesian components $\mathcal{C}_{ijkl}A_{kl}$. We use Div and D to denote the three-dimensional divergence and gradient operators, respectively; div and ∇ are reserved for their two-dimensional counterparts. For example, $\mathrm{Div}\,\mathbf{A} = A_{ij,j}\mathbf{e}_i$ and $\mathrm{div}\,\mathbf{A} = A_{i\alpha,\alpha}\mathbf{e}_i$, where $\{\mathbf{e}_i\}$ is a fixed orthonormal basis and subscripts preceded by commas are used to denote partial derivatives with respect to Cartesian coordinates.

2.2. The order—h^3 energy

The potential energy of an edge-loaded plate of thickness h, apart from an error of order $o(h^3)$, is given by (see Eqs. (111) and (131) of (Steigmann, 2010))

$$E = \int_{\Omega} \overline{W}\,da + \tfrac{1}{24}h^3 \int_{\partial\Omega_e} \mathbf{P1}\boldsymbol{\nu}\cdot\mathbf{g}\,ds, \tag{1}$$

with

$$\overline{W} = h\mathcal{W}(\mathbf{F}) + \tfrac{1}{24}h^3\mathcal{M}(\mathbf{F})[\mathbf{F}']\cdot\mathbf{F}', \tag{2}$$

and

$$\mathbf{F} = \nabla\mathbf{r} + \mathbf{d}\otimes\mathbf{k}, \quad \mathbf{F}' = \nabla\mathbf{d} + \mathbf{g}\otimes\mathbf{k}, \tag{3}$$

where $\mathbf{r}(\mathbf{u})$ is the position of a material point on the deformed image ω of the midplane Ω, ∇ is the gradient operation on Ω, $\nabla\mathbf{r}$ maps Ω to the tangent plane T_ω to the deformed surface ω at the material point $\mathbf{u}$, and the functions $\mathbf{d}(\mathbf{u})$, $\mathbf{g}(\mathbf{u})$ and $\mathbf{h}(\mathbf{u})$ are the *directors*. Here primes refer to through-thickness derivatives, evaluated on the undeformed midplane in the direction of its unit normal $\mathbf{k}$, and $\mathbf{u}$ is position on this plane. In particular, if $\chi(\mathbf{x})$ is the three-dimensional deformation, then $\mathbf{r} = \chi_{|\Omega}$, while $\mathbf{d}$ and $\mathbf{g}$ are equal to χ' and χ'' respectively. Further, $\mathcal{W}(\mathbf{F})$, $\mathbf{P} = \mathcal{W}_{\mathbf{F}}$ and $\mathcal{M}(\mathbf{F}) = \mathcal{W}_{\mathbf{FF}}$ respectively are the restrictions to Ω of the three-dimensional strain-energy function, the Piola stress and the elastic moduli.

We suppose that $\partial\Omega$ consists of possibly overlapping arcs $\partial\Omega_e$ and $\partial\Omega_n$, where essential and natural boundary conditions, respectively, are specified; $\boldsymbol{\nu}$ is the exterior unit normal to $\partial\Omega$ lying to the right of Ω as it is traversed in the sense of Green's theorem. The integral over $\partial\Omega_e$ in (1), which is non-standard, is explained in Steigmann (2010).

In (3), $\mathbf{d}$ and $\mathbf{g}$ are given respectively by the solutions to Steigmann (2010)

$$\left\{\frac{\partial\mathcal{W}}{\partial\tilde{\mathbf{F}}}(\nabla\mathbf{r} + \mathbf{d}\otimes\mathbf{k})\right\}\mathbf{k} = \mathbf{0} \tag{4}$$

and

$$\{\mathbf{A}_{(\mathbf{k})}(\nabla\mathbf{r} + \mathbf{d}\otimes\mathbf{k})\}\mathbf{g} = -\{\mathcal{M}(\nabla\mathbf{r} + \mathbf{d}\otimes\mathbf{k})[\nabla\mathbf{d}]\}\mathbf{k}, \tag{5}$$

where $\mathbf{A}_{(\mathbf{k})}$ is the acoustic tensor defined by

$$\{\mathbf{A}_{(\mathbf{k})}(\mathbf{F})\}\mathbf{v} = \{\mathcal{M}(\mathbf{F})[\mathbf{v}\otimes\mathbf{k}]\}\mathbf{k}. \tag{6}$$

Eq. (4) is simply the usual plane-stress condition, which is shown in Steigmann (2010) to be necessary at the considered order in h if the deformation is to minimize energy. It yields $\mathbf{d}$ uniquely in terms of $\nabla\mathbf{r}$ if the strong-ellipticity condition

$$\mathbf{a}\otimes\mathbf{b}\cdot\mathcal{M}(\tilde{\mathbf{F}})[\mathbf{a}\otimes\mathbf{b}] > 0 \tag{7}$$

is satisfied for all $\mathbf{a}\otimes\mathbf{b} \neq \mathbf{0}$ (Hilgers and Pipkin, 1996). Eq. (5) then delivers $\mathbf{g}$ uniquely in terms of $\nabla\mathbf{r}$ and $\nabla\nabla\mathbf{r}$, implying, as in classical plate theory, that E is specified entirely in terms of the mid-plane deformation function $\mathbf{r}(\mathbf{u})$.

Before proceeding, we introduce the mild constitutive hypothesis that the strain-dependent energy

$$\mathcal{U}(\mathbf{E}) = \mathcal{W}(\mathbf{F}), \tag{8}$$

where

$$\mathbf{E} = \tfrac{1}{2}\left(\mathbf{F}^t\mathbf{F} - \mathbf{I}\right) \tag{9}$$

and $\mathbf{I}$ is the identity for 3-space, is convex in a neighborhood of the origin in strain space, with the origin furnishing an isolated local minimum. Accordingly, the second Piola–Kirchhoff stress,

$$\mathbf{S} = \mathcal{U}_{\mathbf{E}}, \tag{10}$$

satisfies

$$\mathbf{S} = \mathcal{C}(\mathbf{0})[\mathbf{E}] + o(|\mathbf{E}|), \tag{11}$$

in which $\mathcal{C}(\mathbf{0})$ is positive definite in the sense that $\mathbf{A}\cdot\mathcal{C}(\mathbf{0})[\mathbf{A}] > 0$ for all non-zero symmetric $\mathbf{A}$, where

$$\mathcal{C}(\mathbf{E}) = \mathcal{U}_{\mathbf{EE}} \tag{12}$$

is the tensor of strain-dependent moduli. The two sets of moduli are related by

$$\mathcal{M}(\mathbf{F})[\mathbf{A}] = \mathbf{AS} + \tfrac{1}{2}\mathbf{F}\mathcal{C}(\mathbf{E})\left[\mathbf{A}^t\mathbf{F} + \mathbf{F}^t\mathbf{A}\right] \tag{13}$$

for any tensor $\mathbf{A}$; this follows easily by differentiating the relation

$$\mathbf{P} = \mathbf{FS}. \tag{14}$$

It follows from (8), (13) and the minor symmetries of $\mathcal{C}$ that

$$\mathcal{M}(\mathbf{I})[\mathbf{A}] = \mathcal{C}(\mathbf{0})[\mathbf{A}] \tag{15}$$

for any $\mathbf{A}$, and hence that our hypotheses yield strong ellipticity at zero strain, a result that is well known in linear elasticity theory. Accordingly, these hypotheses are compatible with (7).

2.3. The leading-order model for combined stretching and wrinkling

In this work we are interested in a regime of deformation for which the membrane and bending energies are of comparable magnitude. These are associated respectively with the order – h and order – h^3 terms in the expression (2) for the strain-energy function. In Hilgers and Pipkin (1996), it is shown that the functional (1) fails to furnish a well-posed minimization problem as it stands if the 2nd Piola–Kirchhoff stress, $\mathbf{S}$, has a negative eigenvalue anywhere in the domain Ω. However, in Steigmann (2013) it is shown that this issue is ameliorated if the state of stress everywhere in the domain is of order $o(1)$, in which case the effect of stress on the order—h^3 term in (2) may be suppressed with no adverse effect on accuracy.

If $|\mathbf{S}| = o(1)$, as supposed, then the error incurred by imposing $\mathbf{S} = \mathbf{0}$ in the coefficients of h^3 in (2) affects the energy at order $o(h^3)$. Accordingly, order—h^3 accuracy is maintained if $\overline{W}$ in (2) is replaced by

$$W = h\mathcal{W}(\mathbf{F}) + \tfrac{1}{24}h^3\mathcal{M}(\mathbf{R})[\mathbf{F}'] \cdot \mathbf{F}', \tag{16}$$

where $\mathbf{R}$ is the rotation factor in the polar decomposition of the deformation gradient. This is justified by the fact that our constitutive hypotheses (11) yield a strain of order $o(1)$ under the present assumption on stress, which yields a correction to (2) of order $o(h^3)$; this is negligible in the order—h^3 truncation of the energy. Using Steigmann (2007)

$$\mathcal{M}(\mathbf{R})[\mathbf{F}'] \cdot \mathbf{F}' = \mathcal{M}(\mathbf{I})[\mathbf{R}^t\mathbf{F}'] \cdot \mathbf{R}^t\mathbf{F}' \tag{17}$$

with (13), together with the minor symmetries of $\mathcal{C}$, we arrive at the form

$$W = h\mathcal{W}(\mathbf{F}) + \tfrac{1}{24}h^3\mathcal{C}(\mathbf{0})\left[\mathbf{R}^t\mathbf{F}'\right] \cdot \mathbf{R}^t\mathbf{F}' \tag{18}$$

of the strain-energy function. This involves $\nabla\mathbf{r}$ in both terms and $\nabla\nabla\mathbf{r}$ in the second term. It is easily verified that the operative Legendre–Hadamard condition (Hilgers and Pipkin, 1992a, 1996), which we do not state here for the sake of brevity, is satisfied without qualification.

In contrast to conventional buckling, stretch-induced wrinkling is a deformation mode in which the stretching and bending energies are of comparable magnitude (Cerda and Mahadevan, 2003). In this mode of deformation the stress scales as h. To see this, suppose

$$\mathbf{S} = h\overline{\mathbf{S}} + o(h), \tag{19}$$

with $\overline{\mathbf{S}}$ independent of h. Our constitutive hypotheses (11) then furnish the strain

$$\mathbf{E} = h\overline{\mathbf{E}} + o(h), \tag{20}$$

where $\overline{\mathbf{E}} = \mathcal{S}[\overline{\mathbf{S}}]$ and $\mathcal{S}$ is the compliance tensor (the inverse of $\mathcal{C}(\mathbf{0})$). The stretching term in the strain energy (18) reduces to

$$h\mathcal{W}(\mathbf{F}) = \tfrac{1}{2}h^3\overline{\mathbf{E}} \cdot \mathcal{C}(\mathbf{0})\left[\overline{\mathbf{E}}\right] + o(h^3), \tag{21}$$

yielding

$$W = h^3\hat{W} + o(h^3), \tag{22}$$

where

$$\hat{W} = \tfrac{1}{2}\overline{\mathbf{E}} \cdot \mathcal{C}(\mathbf{0})\left[\overline{\mathbf{E}}\right] + \tfrac{1}{24}\mathbf{R}^t\mathbf{F}' \cdot \mathcal{C}(\mathbf{0})\left[\mathbf{R}^t\mathbf{F}'\right]. \tag{23}$$

This incorporates bending and stretching effects at leading order.

In the case of isotropy, to which attention is confined in this work, this strain-energy function reduces to Steigmann (2013)

$$W = \frac{1}{2}h\left\{\frac{2\lambda\mu}{\lambda+2\mu}(\operatorname{tr}\boldsymbol{\epsilon})^2 + 2\mu|\boldsymbol{\epsilon}|^2\right\} + \tfrac{1}{24}h^3\left\{\frac{2\lambda\mu}{\lambda+2\mu}(\operatorname{tr}\boldsymbol{\kappa})^2 + 2\mu|\boldsymbol{\kappa}|^2\right\}, \tag{24}$$

in which the superposed caret has been suppressed, λ and μ are the classical Lamé moduli, satisfying the inequalities $3\lambda+2\mu>0$ and $\mu>0$ associated with the positivity of $\mathcal{C}(\mathbf{0})$,

$$\boldsymbol{\epsilon}=E_{\alpha\beta}\mathbf{e}_\alpha\otimes\mathbf{e}_\beta \tag{25}$$

is the in-plane part of the strain tensor and

$$\boldsymbol{\kappa}=-(\nabla\mathbf{r})^t\mathbf{b}(\nabla\mathbf{r}), \tag{26}$$

where $\mathbf{b}$ is the curvature tensor on the deformed surface, is the bending strain. In terms of Cartesian coordinates on Ω,

$$\boldsymbol{\kappa}=-b_{\alpha\beta}\mathbf{e}_\alpha\otimes\mathbf{e}_\beta;\quad b_{\alpha\beta}=n_i r_{i,\alpha\beta}, \tag{27}$$

where $\mathbf{n}$ is the unit-normal field on the deformed surface and subscripts preceded by commas refer to partial derivatives with respect to the coordinates.

Eq. (24) is precisely Koiter's expression, specialized to flat plates, for the strain energy of a nonlinearly elastic shell (Koiter, 1960, 1966).

In summary, the potential energy $\mathcal{E}$ associated with global stretching-wrinkling in a thin plate of thickness h is given by

$$\mathcal{E}/h^3=E+o(h^3)/h^3, \tag{28}$$

where

$$E=\int_\Omega \hat{W}\,da, \tag{29}$$

with $\hat{W}$ given by (24). Here we have used the fact that $|\mathbf{P}|=O(h)$ to suppress the order $o(h^3)$ contribution of the integral over $\partial\Omega_e$ in (1). Eq. (29) is the leading order potential energy of the plate under the present hypotheses.

Our results indicate that Koiter's model furnishes the leading-order energy in deformations for which the bending and stretching energies are of equal order; this is precisely the regime of interest in this work. Further, in view of (28) it would be possible to regard E as the rigorous leading-order energy if the estimate (19) on the (plane) stress could be established *a priori* in the interior of Ω. We know of no rigorous justification for this assumption, however. This state of affairs notwithstanding, Ciarlet (2005) has given convincing arguments in favor of the Koiter energy as the best overall model of a thin sheet, insofar as the membrane-dominated and bending-dominated regimes are concerned. Our results regarding the intermediate regime in which both effects are equally important lends further support to this view. We observe that in this case there are no small parameters in the leading-order energy functional and hence no localized boundary-layer effects of the kind traditionally associated with bending; instead, in this regime bending is widespread throughout the interior of the sheet.

Remark. Despite its status as the leading-order estimate of the three-dimensional energy in the regime of equal contributions from membrane and bending behavior, the isotropic Koiter model satisfies only the non-strict version of the relevant Legendre–Hadamard necessary condition for energy minimizers (Hilgers and Pipkin, 1996; Steigmann, 2010), and therefore fails to satisfy the hypotheses of available existence theorems based on the direct method of the calculus of variations. Of course this does not mean that minimizers fail to exist, either for the Koiter model or for its three-dimensional antecedent. In this regard we note that an existence theorem for the Koiter energy was recently given in Ciarlet and Mardare (2012), using a large-strain extension of the energy (24). However, we are unaware of any existence results for the energy (24) *per se*. This state of affairs provides further impetus for the use of dynamic relaxation, whereby the problem is regularized by embedding it in a dynamical system with positive-definite mass.

2.4. Euler equations and boundary conditions

The Euler equations for (29) are derived in the manner discussed in Hilgers and Pipkin (1992b). They are

$$\operatorname{div}\mathbf{T}=\mathbf{0}\quad\text{or}\quad T_{i\alpha,\alpha}=0, \tag{30}$$

where $\mathbf{T}$ is the tensor with nontrivial components

$$T_{i\alpha}=N_{i\alpha}-M_{i\alpha\beta,\beta}, \tag{31}$$

and where

$$N_{i\alpha}=\partial W/\partial r_{i,\alpha}\quad\text{and}\quad M_{i\alpha\beta}=\partial W/\partial r_{i,\alpha\beta}, \tag{32}$$

with W given by (22) and r_i the components of the vector, $\mathbf{r}(\mathbf{u})$.

In this work we consider non-standard mixed problems in which position and orientation data are assigned on $\partial\Omega_e$, with vanishing tractions and bending moments assigned on $\partial\Omega_n$. Typical boundary conditions on $\partial\Omega_e$ entail the specification of the position $\mathbf{r}$ and its normal derivative $\mathbf{r}_{,\nu}$. Typical boundary conditions on $\partial\Omega_n$ are Steigmann (2010)

$$T_{i\alpha}\nu_\alpha-(M_{i\alpha\beta}\nu_\alpha\tau_\beta)_{,s}=f_i\quad\text{and}\quad M_{i\alpha\beta}\nu_\alpha\nu_\beta=c_i, \tag{33}$$

where f_i and c_i are the force and couple per unit length, assumed here to vanish. If $\partial\Omega_n$ is piecewise smooth, with a finite number of points where its unit tangent $\boldsymbol{\tau}$ is discontinuous, then the foregoing must be amended to include corner forces

$F_j = [M_{j\alpha\beta}\nu_\alpha\tau_\beta]$, where the bracket identifies the jump of the enclosed quantity occurring as $\partial\Omega_n$ is traversed clockwise. This is explained in detail in Steigmann (2010).

In the present work all examples meet one of the following sets of boundary conditions:

- r_i and $r_{i,\nu}$ assigned on $\partial\Omega_e$, $f_i = 0$ and $c_i = 0$ on $\partial\Omega_n$
- r_i assigned on $\partial\Omega_e$, $f_i = 0$ on $\partial\Omega_n$, and $c_i = 0$ on all of $\partial\Omega$,

corresponding, respectively, to mixed zero-load problems in which part of the boundary is either clamped or pinned. We note that the latter data admit comparisons with simulations based on pure membrane theory.

Regarding the response functions $N_{i\alpha}$ and $M_{i\alpha\beta}$ occurring in (31), we observe that W involves $\nabla\nabla\mathbf{r}$ via $\boldsymbol{\kappa}$. Using (24) and (27) in (32), we derive

$$M_{i\alpha\beta} = \tfrac{1}{12}h^3 n_i\left(\frac{2\lambda\mu}{\lambda+2\mu}b_{\gamma\gamma}\delta_{\alpha\beta} + 2\mu b_{\alpha\beta}\right). \tag{34}$$

On the other hand, $\nabla\mathbf{r}$ is involved in the membrane energy and also in $\boldsymbol{\kappa}$, via the normal $\mathbf{n}$. Using (24) and (27) to evaluate the associated derivative (see Steigmann and Ogden, 1999 for a detailed calculation), we obtain

$$N_{i\alpha} = h\partial\mathcal{W}/\partial r_{i,\alpha} - M_{i\lambda\mu}\Gamma_{\alpha\lambda\mu}, \tag{35}$$

where $\Gamma_{\alpha\lambda\mu}$ are the Christoffel symbols induced by the parametrization of the deformed surface in terms of the coordinates u_α, and

$$\partial\mathcal{W}/\partial r_{i,\alpha} = r_{i,\beta}S_{\beta\alpha} \quad \text{with } S_{\beta\alpha} = \frac{2\lambda\mu}{\lambda+2\mu}E_{\gamma\gamma}\delta_{\beta\alpha} + 2\mu E_{\beta\alpha} \tag{36}$$

the midplane components of the 2nd Piola–Kirchhoff stress.

It is well known that the Christoffel symbols depend on the surface metric $r_{i,\alpha}r_{i,\beta}$ and its coordinate derivatives (Sokolnikoff, 1951). Explicitly,

$$\Gamma_{\alpha\lambda\mu} = E_{\mu\alpha,\lambda} + E_{\alpha\lambda,\mu} - E_{\lambda\mu,\alpha}, \tag{37}$$

where

$$E_{\alpha\beta} = \tfrac{1}{2}\left(r_{i,\alpha}r_{i,\beta} - \delta_{\alpha\beta}\right), \tag{38}$$

in which δ is the Kronecker delta, and the strain itself has been neglected in the computation of $\Gamma_{\alpha\lambda\mu}$ to ensure consistency with (18). Accordingly, strain-gradient effects enter the model via the $\Gamma_{\lambda\alpha\beta}$, whereas bending effects are of course accounted for by the $b_{\alpha\beta}$. The former effect is due to the fact that the variables and differential operators appearing in (31) and (32) involve coordinates in the undeformed configuration, whereas the customary form of the equations involves covariant differentiation on the deformed surface (Koiter, 1966); the transformation from the latter to the former amounts to a strain-gradient effect. We observe that the associated term in (35) is inherently nonlinear and so does not appear in the linearization of the model with respect to the midplane displacement field $\mathbf{r}(\mathbf{u}) - \mathbf{u}$.

Further, we use $(33)_2$ and (34) to write $\mathbf{c} = M\mathbf{n}$ with $M = n_i M_{i\alpha\beta}\nu_\alpha\nu_\beta$. This is shown to yield the interpretation of M as a pure bending moment along the edge of the deformed plate (Steigmann, 2013). Accordingly, the couple $\mathbf{c}$ vanishes if and only if $M = 0$. Parts of the boundary where this condition obtains are either free or pinned.

3. Numerical implementation

In this section we provide a detailed description of a numerical strategy that can be used to solve a variety of problems involving wrinkling with the model described in Section 2. Several such examples will be shown in Section 4. Here, we choose a method known as *dynamic relaxation*, which has proved to be a robust numerical tool for predicting a host of equilibrium phenomena in nonlinear elasticity including cables and membranes (Silling, 1988, 1989; Shugar, 1990; Haseganu and Steigmann, 1994; Taylor and Steigmann, 2009; Rezaiee-pajand et al., 2011; Rodriguez et al., 2011). Our purpose in this section is to construct a surrogate dynamical system which exhibits solutions to (30) as equilibria and, in addition, possesses a mechanical energy that furnishes a Lyapunov function for the associated dynamics. In this way the equilibrium problem is effectively replaced, strictly for purposes of numerical solution, by an *artificial* dynamical system whose equilibria are solutions to the original problem. The desired equilibria are then obtained by a time-stepping procedure that progresses until the energy associated with the surrogate dynamical system is dissipated.

3.1. A dissipative dynamical system

The total mechanical energy of the surrogate dynamical system is given by $E+K$, where E is the strain energy and K is the kinetic energy. Using (31), the time derivative of the strain energy E is easily shown to be expressible in the form

$$\dot{E} = \int_\Omega (\varphi_{\alpha,\alpha} - \dot{r}_i T_{i\alpha,\alpha})\, da, \tag{39}$$

where $\dot{r}_i = \partial r_i(u_\alpha, t)/\partial t$ – the material derivative of the position field – is the velocity of a point on the plate midplane, and

$$\varphi_\alpha = T_{i\alpha}\dot{r}_i + M_{i\alpha\beta}\dot{r}_{i,\beta}. \tag{40}$$

The first term in the integrand of (39) is transformed via Green's theorem, using the decomposition

$$\nabla \mathbf{r} = \mathbf{r}_{,s} \otimes \boldsymbol{\tau} + \mathbf{r}_{,\nu} \otimes \boldsymbol{\nu}, \tag{41}$$

where $\boldsymbol{\tau}$ and $\boldsymbol{\nu}$ are the unit tangent and normal to the edge and the tangential derivative $\mathbf{r}_{,s}$ is obtained by differentiating $\mathbf{r}$ with respect to arclength on $\partial\Omega$. Integrating by parts with respect to arclength on $\partial\Omega$, we derive

$$\int_\Omega \varphi_{\alpha,\alpha}\, da = \int_{\partial\Omega} \varphi_\alpha \nu_\alpha\, ds = \int_{\partial\Omega_n} (f_i\dot{r}_i + c_i\dot{r}_{i,\nu})\, ds, \tag{42}$$

where

$$\dot{r}_{i,\nu} = \dot{F}_{i\alpha}\nu_\alpha \tag{43}$$

is the normal derivative of the velocity. Thus, (39) becomes

$$\dot{E} = \int_{\partial\Omega_n} (f_i\dot{r}_i + c_i\dot{r}_{i,\nu})\, ds - \int_\Omega \dot{r}_i T_{i\alpha,\alpha}\, da. \tag{44}$$

If the boundary of the sheet has corners, then the associated corner forces will in general contribute to the rate of change of the energy. However, in this study the work-conjugate velocities at corners, if any, vanish identically; accordingly, corner forces make no contribution to the energetics in the examples considered.

Proceeding, we take the kinetic energy, K, of the surrogate dynamical problem to be

$$K = \tfrac{1}{2}\int_\Omega \rho|\dot{\mathbf{r}}|^2\, da, \tag{45}$$

where $\mathbf{r}(\mathbf{u}, t) = r_i(\mathbf{u}, t)\mathbf{e}_i$ is the position vector of a point on the deformed midsurface and ρ is the areal mass density of the sheet on the reference midsurface. We emphasize that this is merely the form of the kinetic energy assumed for the surrogate dynamical system; the kinetic energy in an actual dynamical theory of plates typically includes a rotatory inertia term and is thus somewhat more complicated. This fact, however, is of no consequence as far as our present objective is concerned.

To extend the dynamic relaxation scheme used in Haseganu and Steigmann (1994) and Taylor and Steigmann (2009) to the present problem in as simple a manner as possible, we follow Silling (1988, 1989) and substitute the surrogate equation of motion

$$T_{i\alpha,\alpha} = \rho\ddot{r}_i + c\dot{r}_i \tag{46}$$

in place of (30), where c is a damping coefficient. The structure of the viscous term implies that this is not a physically meaningful equation of motion; actual viscous effects would have to be accommodated via the constitutive theory for the sheet. However, we will show that (45) and (46) generate a Lyapunov function for the surrogate dynamical system. To this end, we observe that taking the inner product of both sides of (46) with $\dot{r}_i$ and integrating over Ω yields (using (45))

$$\int_\Omega \dot{r}_i T_{i\alpha,\alpha}\, da = \dot{K} + \int_\Omega c|\dot{\mathbf{r}}|^2\, da. \tag{47}$$

Recall the boundary conditions (33), where we assume that the components of applied force, f_i, and couple, c_i, per unit length are zero. In Section 3.3, we develop a procedure to impose $(33)_1$ automatically at every instant in time, whereas $(33)_2$ is recovered only after the transient response has run its course. With this in mind, we put $f_i = 0$ in (44) and combine with (47) to derive

$$(E+K)^{\cdot} = \int_{\partial\Omega_n} c_i\dot{r}_{i,\nu}\, ds - \int_\Omega c|\dot{\mathbf{r}}|^2\, da. \tag{48}$$

For the purpose of ensuring that the surrogate energy E is dissipated in the course of the transient dynamics, we impose

$$c_i = -c\dot{r}_{i,\nu} \quad \text{on } \partial\Omega_n, \tag{49}$$

yielding

$$(E+K)^{\cdot} = -c\left(\int_{\partial\Omega_n} |\dot{\mathbf{r}}_{,\nu}|^2\, ds + \int_\Omega |\dot{\mathbf{r}}|^2\, da\right), \tag{50}$$

and ensuring, for positive c, that the energy is strictly decreasing as long as the velocity is non-zero anywhere in Ω and the rotational velocity is non-zero anywhere on $\partial\Omega_n$. Moreover, the energy $E+K$ reduces to E in equilibrium states, and thus furnishes a Lyapunov function for the dynamical system provided that equilibria are minimizers of the overall strain energy. Strictly, these remarks apply to finite-dimensional systems and hence to the discretized surrogate dynamical system described in Section 3.2.

3.2. Finite-difference discretization

In this section, (46) is discretized by using a finite-difference scheme derived from Green's theorem. The application of this scheme to plane-strain problems in nonlinear elasticity theory is described by Silling (1989) and its adaptation to membrane theory is developed in Haseganu and Steigmann (1994) and Taylor and Steigmann (2009). Here, we summarize the method and describe its extension to the present theory.

3.2.1. Spatial discretization of the equations of motion

We spatially discretize the basic system of equilibrium equations given by (30). To this end, we cover the reference plane Ω by a mesh consisting of two types of points: *nodes* and *zone-centered points*. A schematic of the mesh is depicted in Fig. 1. Nodes are labelled using integer superscripts (i,j). Thus, $u_\alpha^{i,j}$ are the referential coordinates of node (i,j), where $u_\alpha = \mathbf{u}\cdot\mathbf{e}_\alpha$ $(\alpha = 1,2)$. The four regions formed by a node, together with its nearest-neighbor nodes, are called *zones*. Zone-centered points, identified by blue circles in the figure, are labelled using half-integer superscripts.

To represent (30) at node (i, j), we first discretize the divergence, $T_{i\alpha,\alpha}$, using Green's theorem applied in the form

$$\int_D T_{i\alpha,\alpha}\, da = e_{\alpha\beta}\int_{\partial D} T_{i\alpha}\, du_\beta, \tag{51}$$

where $e_{\alpha\beta}$ is the unit alternator ($e_{12} = -e_{21} = 1,\ e_{11} = e_{22} = 0$) and D is identified with the quadrilateral contained within the dashed contour of Fig. 1. The left-hand side of (51) is estimated as the nodal value of the integrand multiplied by the area of D; the right-hand side as the zone-centered values of the integrand on each of the four edges of ∂D multiplied by the appropriate edge length. Thus Silling (1988),

$$\begin{aligned} 2A^{i,j}(T_{k\alpha,\alpha})^{i,j} = e_{\alpha\beta}[&T_{k\alpha}^{i+1/2,j+1/2}(u_\beta^{i,j+1} - u_\beta^{i+1,j}) + T_{k\alpha}^{i-1/2,j+1/2}(u_\beta^{i-1,j} - u_\beta^{i,j+1}) \\ &+ T_{k\alpha}^{i-1/2,j-1/2}(u_\beta^{i,j-1} - u_\beta^{i-1,j}) + T_{k\alpha}^{i+1/2,j-1/2}(u_\beta^{i+1,j} - u_\beta^{i,j-1})], \end{aligned} \tag{52}$$

where

$$A^{i,j} = \tfrac{1}{4}\left[\left(u_2^{i-1,j} - u_2^{i+1,j}\right)\left(u_1^{i,j+1} - u_1^{i,j-1}\right) - \left(u_1^{i-1,j} - u_1^{i+1,j}\right)\left(u_2^{i,j+1} - u_2^{i,j-1}\right)\right] \tag{53}$$

is one-half the area of the quadrilateral. The discretized version of (30) is then given by

$$\Sigma_k^{i,j} = 0, \tag{54}$$

where

$$\Sigma_k^{i,j} = 2A^{i,j}(T_{k\alpha,\alpha})^{i,j}. \tag{55}$$

To evaluate the right-hand side we require $T_{k\alpha}$ at the zone-centered points (cf. (52)). This in turn requires the zone-centered values of $N_{k\alpha}$ and $M_{i\alpha\beta,\beta}$ (cf. (31)). The components $N_{k\alpha}$ are determined by the constitutive equation (36) together with the zone-centered deformation gradient. To compute the deformation gradient, we use Green's theorem in the form

$$\int_D F_{i\alpha}\, da = e_{\alpha\beta}\int_{\partial D} r_i\, du_\beta. \tag{56}$$

We now identify D with the shaded region in Fig. 1. The left-hand side is approximated by the product of the shaded area with the integrand, evaluated at the zone-centered point, and the four edge contributions to the right-hand side are approximated by replacing the integrand in each with the average of the nodal values at the endpoints. This gives

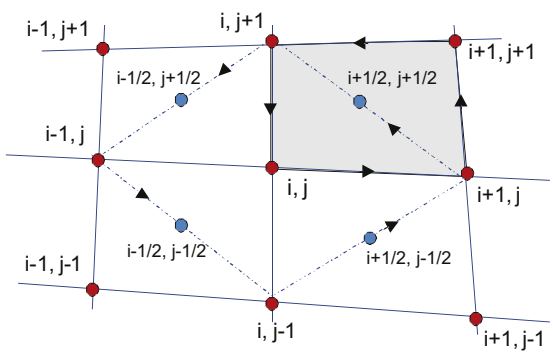

Fig. 1. Stencil of the finite-difference mesh. Nodes shown as red circles. Area colored gray denotes a *zone* with blue circles representing zone-centered points. Contours marked with arrows denote regions of approximate integration. (For interpretation of the references to color in this figure caption, the reader is referred to the web version of this paper.)

(Silling, 1988)

$$2A^{i+1/2,j+1/2}(F_{k\alpha}^{i+1/2,j+1/2}) = e_{\alpha\beta}[(r_k^{i+1,j+1} - r_k^{i,j})(u_\beta^{i,j+1} - u_\beta^{i+1,j}) - (r_k^{i,j+1} - r_k^{i+1,j})(u_\beta^{i+1,j+1} - u_\beta^{i,j})], \tag{57}$$

where

$$A^{i+1/2,j+1/2} = \tfrac{1}{2}\left[\left(u_2^{i,j+1} - u_2^{i+1,j}\right)\left(u_1^{i+1,j+1} - u_1^{i,j}\right) - \left(u_1^{i,j+1} - u_1^{i+1,j}\right)\left(u_2^{i+1,j+1} - u_2^{i,j}\right)\right]. \tag{58}$$

The components $M_{i\alpha\beta,\beta}$ can be computed by using (57), with $F_{k\alpha}$ replaced by $M_{k\alpha\beta,\beta}$ and r_k by $M_{k\alpha\beta}$; thus,

$$2A^{i+1/2,j+1/2}(M_{k\alpha\beta,\beta}^{i+1/2,j+1/2}) = e_{\beta\gamma}[(M_{k\alpha\beta}^{i+1,j+1} - M_{k\alpha\beta}^{i,j})(u_\gamma^{i,j+1} - u_\gamma^{i+1,j}) - (M_{k\alpha\beta}^{i,j+1} - M_{k\alpha\beta}^{i+1,j})(u_\gamma^{i+1,j+1} - u_\gamma^{i,j})], \tag{59}$$

wherein the right-hand side involves the nodal values of $M_{k\alpha\beta}$. These in turn are determined constitutively (cf. (34)) by the nodal values of the surface normal and curvature $b_{\alpha\beta}$, given by

$$b_{\alpha\beta}^{i,j} = n_k^{i,j} F_{k\alpha,\beta}^{i,j}, \tag{60}$$

where

$$\begin{aligned} 2A^{i,j}F_{k\alpha,\beta}^{i,j} = e_{\beta\gamma}[&F_{k\alpha}^{i+1/2,j+1/2}(u_\gamma^{i,j+1} - u_\gamma^{i+1,j}) + F_{k\alpha}^{i-1/2,j+1/2}(u_\gamma^{i-1,j} - u_\gamma^{i,j+1}) \\ &+ F_{k\alpha}^{i-1/2,j-1/2}(u_\gamma^{i,j-1} - u_\gamma^{i-1,j}) + F_{k\alpha}^{i+1/2,j-1/2}(u_\gamma^{i+1,j} - u_\gamma^{i,j-1})]. \end{aligned} \tag{61}$$

The exact expression for $F_{k\alpha,\beta}$ is symmetric in the second pair of subscripts. We impose this by identifying $F_{k\alpha,\beta}^{i,j}$ with $\frac{1}{2}\left(F_{k\alpha,\beta}^{i,j} + F_{k\beta,\alpha}^{i,j}\right)$.

The expression (60) for the curvature involves the unit normal to the deformed plate surface, which also occurs explicitly in (34). This is given analytically by (Taylor and Steigmann, 2009)

$$\alpha n_k = \tfrac{1}{2} e_{ijk} e_{\alpha\beta} r_{i,\alpha} r_{j,\beta} \tag{62}$$

in which α – the areal stretch – is the norm of the right-hand side. Thus we compute

$$(\alpha n_k)^{i+1/2,j+1/2} = \tfrac{1}{2} e_{ijk} e_{\alpha\beta} F_{i\alpha}^{i+1/2,j+1/2} F_{j\beta}^{i+1/2,j+1/2}, \quad \text{etc} \qquad ., \tag{63}$$

and use the average of these to obtain the nodal value for use in (60):

$$(\alpha n_k)^{i,j} = \tfrac{1}{4}\left[(\alpha n_k)^{i-1/2,j+1/2} + (\alpha n_k)^{i+1/2,j+1/2} + (\alpha n_k)^{i-1/2,j-1/2} + (\alpha n_k)^{i-1/2,j-1/2}\right], \tag{64}$$

where $(\alpha^{i,j})^2 = (\alpha n_k)^{i,j}(\alpha n_k)^{i,j}$.

Lastly, the zone-centered values of $N_{k\alpha}$, required in (54), involve the associated Christoffel symbols $\Gamma_{\alpha\lambda\mu}$. These are approximated by

$$\Gamma_{\alpha\lambda\mu} = F_{k\alpha} F_{k\lambda,\mu}, \tag{65}$$

which is consistent with the null-strain values adopted in (37). The $\Gamma_{\alpha\lambda\mu}^{i+1/2,j+1/2}$, etc., required in (54), are obtained using the zone-centered deformation gradient together with the average of the $F_{k\lambda,\mu}$ at the adjacent nodes.

To solve (54) we replace it by the artificial dynamical system (cf. (46))

$$\Sigma_k^{i,j,n} = m^{i,j}\ddot{r}_k^{i,j,n} + c^{i,j}\dot{r}_k^{i,j,n}, \tag{66}$$

where $m^{i,j} = 2A^{i,j}\rho$ is the nodal mass, $c^{i,j} = 2A^{i,j}c$ is the nodal damping coefficient, n is the time step, and superposed dots refer to derivatives with respect to (artificial) time. This is *not* the discrete form of the actual dynamical equations. Rather, it is an artificial system introduced solely to expedite the computation of equilibria.

3.2.2. Temporal discretization

The time derivatives in (66) are approximated by the central differences

$$\dot{r}_k^n = \tfrac{1}{2}\left(\dot{r}_k^{n+1/2} + \dot{r}_k^{n-1/2}\right), \quad \ddot{r}_k^n = \tfrac{1}{h}\left(\dot{r}_k^{n+1/2} - \dot{r}_k^{n-1/2}\right), \quad \dot{r}_k^{n-1/2} = \tfrac{1}{h}\left(r_k^n - r_k^{n-1}\right), \tag{67}$$

where h is the time increment and the node label (i, j) has been suppressed. Substitution into (66) furnishes the explicit, decoupled system

$$(h^{-1} + c/2)m^{i,j}\dot{r}_k^{i,j,n+1/2} = (h^{-1} - c/2)m^{i,j}\dot{r}_k^{i,j,n-1/2} + \Sigma_k^{i,j,n}, \quad r_k^{i,j,n+1} = r_k^{i,j,n} + h\dot{r}_k^{i,j,n+1/2}, \tag{68}$$

which is used to advance the solution in time node-by-node. We remark that because only long-time limits of solutions are relevant, temporal accuracy is not an issue. Stability is dependent on h, c, and $m^{i,j}$ via the system stiffness (Shugar, 1990; Topping and Khan, 1994; Rezaiee-pajand et al., 2011).

3.2.3. Numerical solution procedure

The starting procedure for (68) is derived from the quiescent initial conditions

$$r_k^{i,j,0} = R_k(u_\alpha^{i,j}), \quad \dot{r}_k^{i,j,0} = 0, \tag{69}$$

where $R_k(u_\alpha)$ is assigned. Thus, from (68) we obtain

$$(2/h)m^{i,j}\dot{r}_k^{i,j,1/2} = \Sigma_k^{i,j,0}, \tag{70}$$

in which the right-hand side is determined by the functions R_k. The system is non-dimensionalized and the solution is advanced to the first t_n such that

$$\max|\Sigma_k^{i,j,n}| < \varepsilon, \tag{71}$$

a suitable tolerance.

In practice, we use an efficient alternative to viscous damping known as *kinetic damping* (Shugar, 1990; Topping and Khan, 1994; Rezaiee-pajand et al., 2011), in which (68) is solved with the viscosity, c, set to zero. At each step, t_n, we compute the total system kinetic energy

$$K^{n+1/2} = \frac{1}{2}\sum_{i,j} m^{i,j}\dot{r}_k^{i,j,n+1/2}\dot{r}_k^{i,j,n+1/2}. \tag{72}$$

If a peak value of the kinetic energy is detected, we compute an associated position field using the estimate

$$r_k^{i,j,p} = r_k^{i,j,n+1} - \frac{3h}{2}\dot{r}_k^{i,j,n+1/2} + \frac{h^2}{2m}\Sigma_k^{i,j,n}, \tag{73}$$

and then restart the procedure with the initial conditions $r_k^{i,j,0} = r_k^{i,j,p}$ and $\dot{r}_k^{i,j,0} = 0$ (Topping and Khan, 1994; Rezaiee-pajand et al., 2011). This method involves only the parameters h and ρ, the latter via $m^{i,j}$. We fix one of these, say $h=1$, and then adjust the other to achieve stability and as rapid a rate of decay as possible, until (71) is achieved.

3.3. Boundary conditions

In this work we simulate mixed problems in which the bending moment and traction vanish on a part of the boundary with the complementary part assumed to be either free or pinned; the latter entails the assignment of position data and null values of the bending moment. As discussed in Section 2.4, this in turn requires that $M_{k\alpha\beta}\nu_\alpha\nu_\beta$ vanish on the relevant part of the boundary. As we are concerned exclusively with equilibria, we enforce this by using a scheme suggested by the energy argument of Section 3.1. Thus, at boundary nodes we impose

$$M_{k\alpha\beta}^{i,j}\nu_\alpha\nu_\beta = -c\dot{F}_{k\alpha}^{i,j}\nu_\alpha, \tag{74}$$

in which the left-hand side is computed as before, using zone-centered values of the deformation gradient exterior to the mesh; these in turn are computed using nodal positions at a layer of nodes exterior to the mesh (Fig. 2).

The right-hand side of (74) is estimated by averaging $\dot{F}_{k\alpha}$ at the exterior zone-centered points adjacent to node (i,j), using (57) in which r_k is replaced by $\dot{r}_k$. Application of the central-difference operators (67) then furnishes an explicit, decoupled

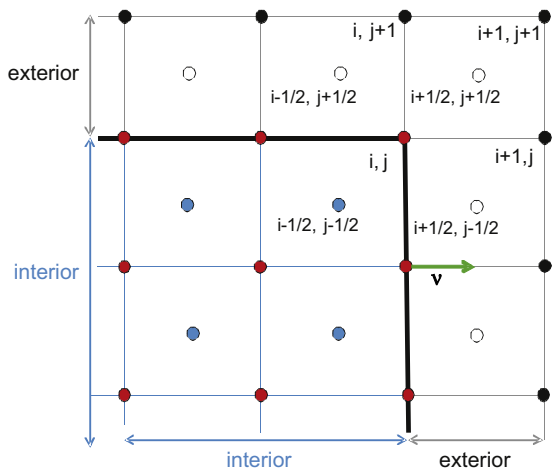

Fig. 2. Schematic of a typical finite-difference mesh at a corner boundary. Nodes and zone-centered points contained within the body are denoted with red and blue circles, respectively. Nodes and zone-centered points exterior to the body are denoted with black and white circles, respectively. Outward unit normal ν indicated with green arrow. (For interpretation of the references to color in this figure caption, the reader is referred to the web version of this paper.)

scheme for updating the external nodal positions. This proceeds in parallel with the computation described in Section 3.2.1 until these nodal positions settle to their static values. In effect the deformations of the exterior nodes simulate the orientation of the tangent plane to the deformed plate required to maintain equilibrium in response to the zero-moment edge condition.

Regarding the traction data, we proceed by integrating (46) over the region D containing a boundary node (Fig. 2), obtaining

$$\int_D (\rho\ddot{r}_k + c\dot{r}_k)\, da = \int_{\partial D_i} T_{k\alpha}\nu_\alpha\, ds + \int_{\partial D_e} T_{k\alpha}\nu_\alpha\, ds, \tag{75}$$

where $\partial D_{i,e}$, respectively, are the internal and external parts of the boundary ∂D. Here we use $(33)_1$ in the integral over ∂D_e, together with $f_k = 0$, obtaining (see Fig. 2)

$$\int_{\partial D_e} T_{k\alpha}\nu_\alpha\, ds = (M_{k\alpha\beta}\nu_\alpha\tau_\beta)^{i,j+1} - (M_{k\alpha\beta}\nu_\alpha\tau_\beta)^{i,j-1}. \tag{76}$$

The interior integral over ∂D_i is approximated as in (52), and the left-hand side of (76) is estimated as before, yielding (66) in which

$$\Sigma_k^{i,j} = e_{\alpha\beta}[T_{k\alpha}^{i-1/2,j+1/2}(u_\beta^{i-1,j} - u_\beta^{i,j+1}) + T_{k\alpha}^{i-1/2,j-1/2}(u_\beta^{i,j-1} - u_\beta^{i-1,j})] + M_{k\alpha\beta}^{i,j+1}\nu_\alpha\tau_\beta - M_{k\alpha\beta}^{i,j-1}\nu_\alpha\tau_\beta. \tag{77}$$

The nodal positions are then updated together with those in the interior until a static configuration is attained.

4. Simulations

In this section, we demonstrate our model via four examples that highlight large elastic deformations in wrinkled thin sheets. These are selected for the purpose of facilitating comparisons with available experimental, numerical, and analytical results. In particular, the examples shown in Sections 4.3 and 4.4 are compared with corresponding results using the much simpler tension-field theory of elastic membranes.

Tension-field theory has the feature that it admits only tensile states of stress, extending the range of applicability of membrane theory to states of strain that would otherwise generate compressive stresses that are unstable in a pure membrane. An extended membrane theory that incorporates tension-field theory automatically may be obtained from the conventional membrane energy (the order—h energy in (24)) via the process of *relaxation*, which entails the construction of an energy minimizing sequence of deformations containing ever-more finely spaced wrinkles (Pipkin, 1986; Dacarogna, 1989). The limit of the sequence is a smooth deformation, and the strain-energy function associated with it is such that compressive stresses are excluded. The theory also emerges from three-dimensional nonlinear elasticity via the method of gamma convergence (LeDret and Raoult, 1995), a technique for extracting the leading-order variational problem in the small-thickness limit. The resulting model is based on a *relaxed* membrane strain-energy function, which is constructed from the original by a straightforward procedure. This procedure, and its application to the present membrane energy (cf. (24)), are thoroughly documented elsewhere (Pipkin, 1986; Haseganu and Steigmann, 1994; Taylor and Steigmann, 2009) and thus simply invoked in the present work without further comment.

Although tension-field theory cannot be used to determine the detailed deformation in a wrinkled region of the sheet, it does yield a prediction of the location and extent of wrinkled regions; these are the regions where the relaxed energy generates purely tensile states of stress or slack states with no stress at all. This information, together with the predicted (tensile) stretch distribution in wrinkled regions, furnishes a basis for direct assessment of tension-field theory against the standard of the more general model adopted here. Accordingly, we present simulations based on tension-field theory alongside those based on the present model.

In all examples we report the Young's modulus, E, and Poisson ratio, ν, of the materials considered. These are connected to the Lamé moduli used in (34) and (36) by the well-known relations

$$2\mu = \frac{E}{1+\nu}, \quad \lambda = \frac{E\nu}{(1-2\nu)(1+\nu)}. \tag{78}$$

Further, we note that in all examples, the equilibria obtained may be regarded as stable relative to perturbations represented by the selected initial conditions. Of course it is not possible to impose infinitely many sets of initial data, and so the equilibria obtained could conceivably be merely conditionally stable.

4.1. Extension of a rectangular silicone rubber sheet

This example is inspired by the theoretical investigations of Cerda and Mahadevan (2003) and Puntel et al. (2011), the experimental and numerical investigation conducted by Zheng (2009), and the numerical studies of Nayyar et al. (2011) and Healey et al. (2013). A rectangular sheet of silicone rubber is considered, with properties $E = 1$ MPa and $\nu = 0.5$ and dimensions of 254 mm $\times$ 101.6 mm with thickness $h = 0.1$ mm (Zheng, 2009). We non-dimensionalize the sheet dimensions using $L = 101.6$ mm. The sheet is pinned along the top and bottom edges and the vertical sides are unloaded. The bottom edge is fixed and the top edge is displaced vertically by varying amounts.

The sheet is discretized using a rectangular mesh that is biased to have a higher concentration of nodes in the central region, where wrinkling is expected to occur. For applied stretches of 10% or less, a mesh refinement study shows that approximately 60,000 nodes yields a converged solution. At larger applied stretches, the large deformation at the corners of the sheet requires a finer mesh. In the present example, we use approximately 120,000 nodes when the applied stretch is larger than 10%. The initial configuration is chosen to coincide with the assigned displacements at the top and bottom boundaries while having a small random out-of-plane perturbation at the interior nodes.

First, we illustrate the kinetic damping process in Fig. 3 for a typical simulation with the sheet stretched by 10%. Here, we present the normalized kinetic energy of the system as a function of dynamic relaxation step, or iteration, with key kinetic energy peaks identified. The configuration at each identified peak is shown demonstrating the progression of the solution from a near initial state (Fig. 3a) to the final equilibrium state (Fig. 3f). For this example, we use a random initial out-of-plane perturbation with a normalized magnitude in the range $(0, 10^{-6})$. Through the first seven kinetic energy peaks, the out-of-plane displacement at each point in the sheet remains at approximately the same order of magnitude (Fig. 3a–b). As the number of iterations increases, we observe the initiation of the wrinkles near the top corners (Fig. 3c). These have out-of-plane displacements several orders of magnitude larger than the initial random perturbation. Like the in-plane displacement, the wrinkles move down the sheet from the top boundary and the wrinkled area become more widespread (Fig. 3c–d–e) while the wrinkles themselves become more ordered until finally settling at the equilibrium configuration (Fig. 3f).

Next, in Fig. 4a–d, we show the equilibrium configurations for the sheet at stretches of 5%, 10%, 20%, and 30%. In addition, we compare the wrinkled cross-sections (at the transverse midplane) of these results (Fig. 4e) with the corresponding experimental and numerical results of Zheng (2009) (Fig. 4f and g). The simulations yield qualitative agreement with Zheng's results as well as the predictions of Cerda and Mahadevan (2003) and Puntel et al. (2011). In particular, wrinkling is mainly confined to the interior of the sheet, with the wrinkle trajectories oriented vertically. Quantitative comparisons with Cerda and Mahadevan (2003) and Puntel et al. (2011) are not appropriate, however, due to the simplifying assumptions on which those theoretical works are based, such as the use of global constraints intended to mimic the neglected boundary conditions. These assumptions facilitate tractable analysis but do not faithfully model the actual boundary conditions which are here modeled explicitly.

In Zheng's numerical results, the wrinkle amplitude at first increases, peaking at a stretch of about 10%, and then decreases until the wrinkles nearly disappear at a stretch of 30% (Fig. 4g). Likewise, our cross-sectional results (Fig. 4e) show similar behavior. This is also in accord with the numerical studies of Nayyar et al. (2011) and Healey et al. (2013).

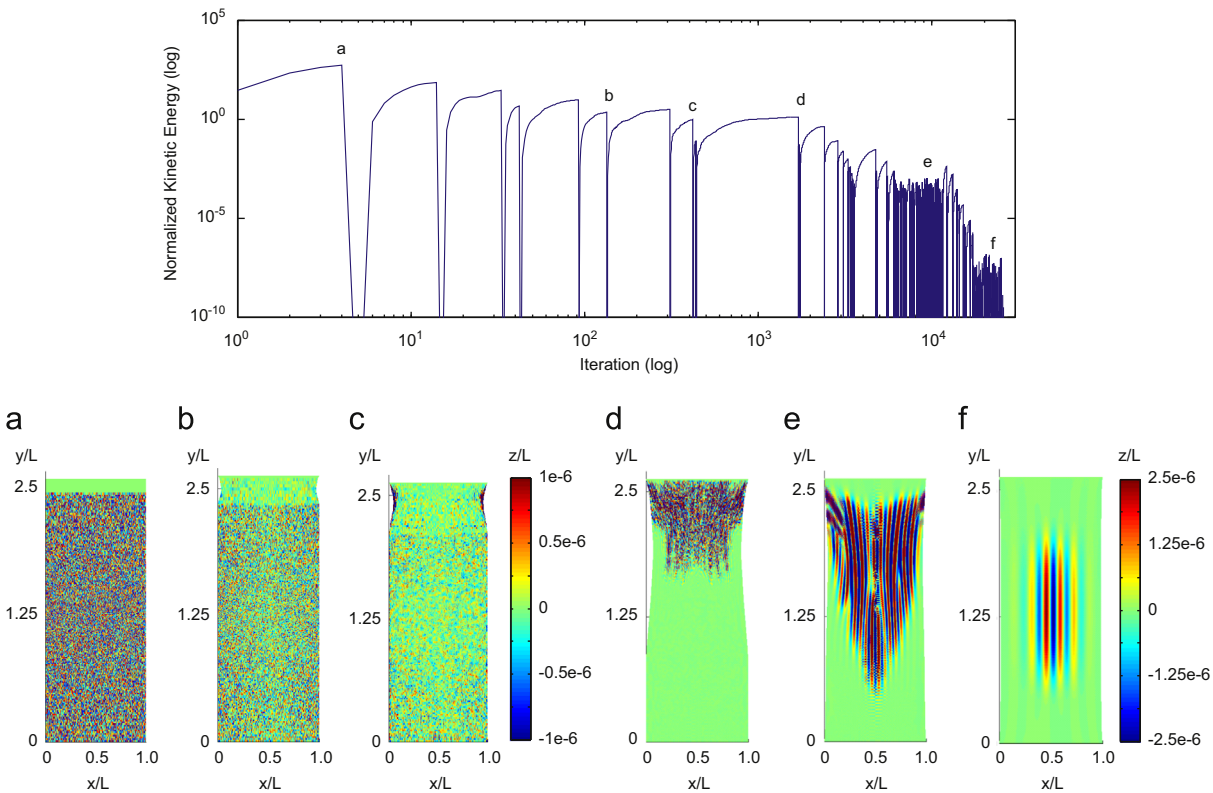

Fig. 3. Typical normalized system kinetic energy as a function of dynamic relaxation iteration for a rectangular silicone rubber sheet undergoing uniaxial tension. Sheet configurations at various points in the kinetic damping process are shown in (a) through (f).

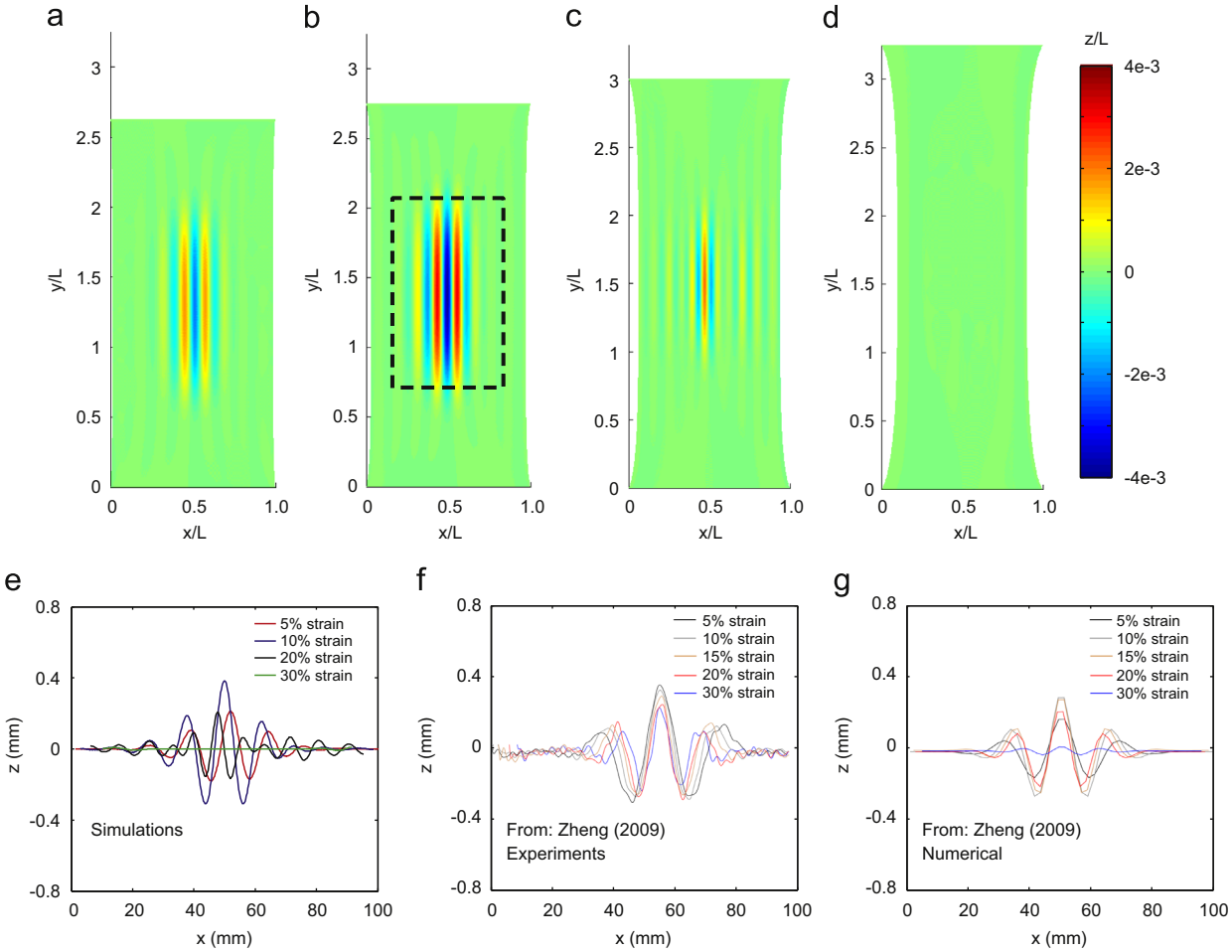

Fig. 4. Equilibrium configuration of sheet undergoing tensile strains of 5% (a), 10% (b), 20% (c), and 30% (d). Wrinkled cross-sectional data (e) of (a)–(d) together with experimental (f) and post-buckling numerical results (g) obtained by Zheng (2009).

In Zheng's experiment (see Fig. 3.22 of Zheng, 2009), the initial unstressed configuration of the silicone rubber sheet is highly wrinkled with the wrinkle trajectories aligned slightly off the vertical axis. Under load, the wrinkles align with the vertical axis, but the wrinkling mode (i.e. the shape of the wrinkled cross-section) remains essentially unchanged from its initial state. The amplitude of the wrinkles generally decreases under increasing load, but never completely disappears (Fig. 4f). In contrast, our model is based on an initially planar reference configuration, making meaningful comparisons with the experiment difficult. Nevertheless, good quantitative agreement is obtained with respect to the general magnitude of the wrinkle amplitudes. Our simulations also predict smaller amplitude wrinkles extending to the free edges as seen experimentally in Fig. 4f, but not present in the numerical results (Fig. 4g).

Zheng's post-buckling numerical results (Fig. 4g) are based on an initial buckling analysis using the finite element method. In a buckling analysis, modes and mode shapes are extracted from the tangent stiffness matrix. This is followed by a geometrically nonlinear post-buckling simulation using some number of the lowest mode shapes as an initial perturbation. The two lowest mode shapes found by Zheng via the buckling analysis occurred at the same eigenvalue—one with a large central peak ("symmetric" mode) and one with two large peaks on either side of the sheet's vertical centerline ("anti-symmetric" mode). The fact that they occur at the same eigenvalue suggests that either shape is equally likely to appear once the critical wrinkling threshold is met. The results of Zheng's post-buckling analysis all fall into the symmetric mode shape based on the selection of only that mode shape as an initial imperfection. In contrast, Healey et al. (2013) determined that there is in fact an entire "orbit" of equally likely neutrally stable configurations that include symmetric and anti-symmetric solutions as well as a family of wrinkle configurations "in-between". Our results fall roughly into both symmetric (strain 10%) and anti-symmetric (strain 20% and 30%) type mode shapes.

To investigate the wrinkling shapes further, we conducted ten simulations at 10% strain with a different initial condition for each. As in the kinetic damping example shown in Fig. 3, each of the ten simulations has a unique initial randomized out-of-plane perturbation. Fig. 5 shows an inset (see Fig. 4b) focusing on the central region of the equilibrium configuration for each case. We identify two families of mode shapes: symmetric (Fig. 5a) and anti-symmetric (Fig. 5b). As shown in Fig. 5c,

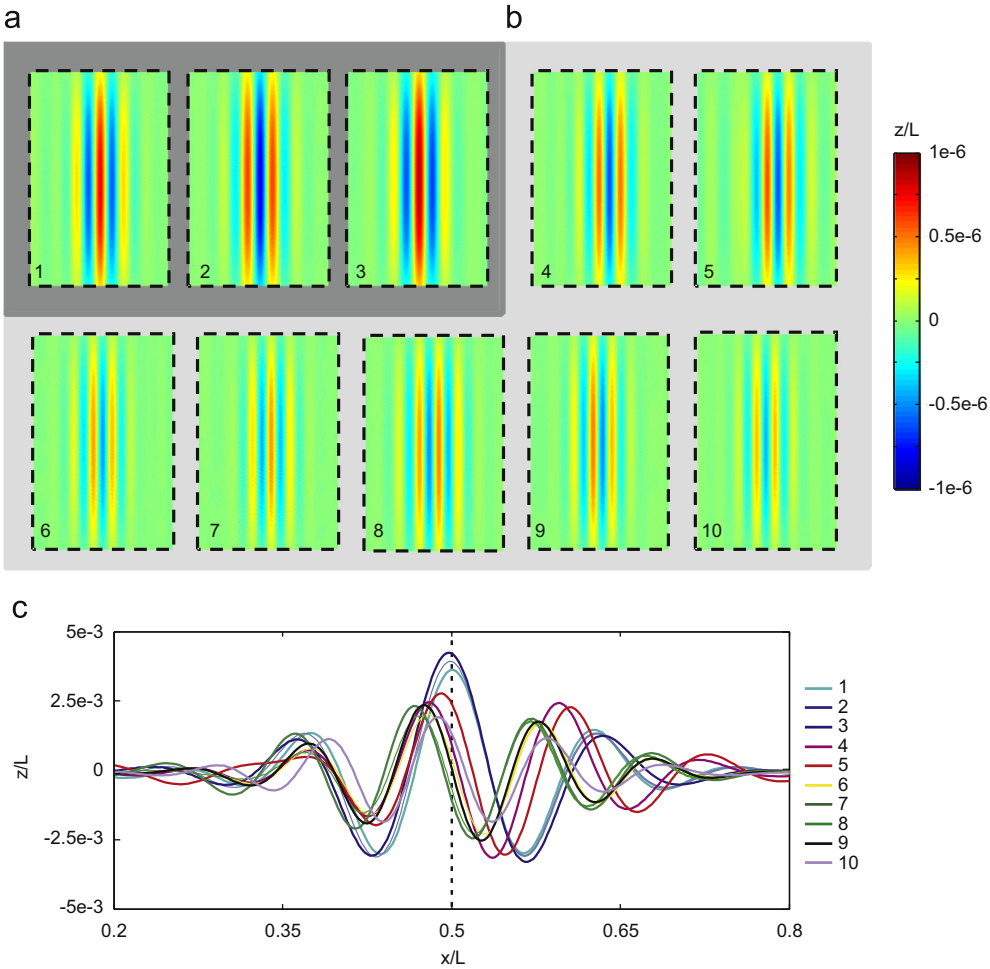

Fig. 5. Central regions (see Fig. 4b for inset area) of silicone rubber sheet in equilibrium at 10% strain starting from ten randomized initial conditions. Two families of modes are identified: symmetric (a) and anti-symmetric (b). The corresponding cross-sectional profiles (c) suggest that a range of equilibrium states exist between symmetric and anti-symmetric states.

our anti-symmetric family actually contains configurations that might be better classified as "in-between" states. For example, the fifth randomized configuration has an anti-symmetric shape that is phase-shifted with respect the center-line. These results are consistent with the analysis of Healey et al. (2013).

4.2. Shearing of a rectangular Kapton sheet

Inspired by the experiments of Wong and Pellegrino (2006a), we simulate the response of a rectangular Kapton sheet clamped along opposite (horizontal) edges, with the remaining (vertical) edges remaining free of load. This is modeled here as a mixed clamped/zero-traction, zero-moment boundary value problem. In principle, the clamping condition entails the specification of the orientation $\mathbf{n}$ on an edge; here, this is simply the unit normal to the initial plane of the sheet. However, in Steigmann (2013) it is shown that this is equivalent, in the order$-h^3$ model considered here, to the specification of the normal derivative $\mathbf{r}_{,\nu}$. If position on the edge is also specified, then it follows from (41) that clamping amounts to the specification of the deformation gradient $F_{i\alpha}$. Accordingly, we specify the deformation gradient on $\partial\Omega_e$, using the procedure described in Section 3.2.

The considered sheet has dimensions 380 mm $\times$ 128 mm, with thickness $h=0.025$ mm, Young's modulus $E=3.5$ GPa and Poisson's ratio $\nu=0.31$ (Wong and Pellegrino, 2006c). We normalize the position and displacement data using $L=380$ mm. The lower edge is fixed and the upper edge undergoes a controlled shear (horizontal) displacement. We consider two examples in which this displacement is either 0.5 mm or 3.0 mm. Our discretization is based on a uniformly spaced rectangular grid of 80,000 nodes. The actual and simulated deformed configurations of the sheet are depicted in the first and second rows, respectively, of Fig. 6. We draw attention to three specific aspects of wrinkling in the deformed configuration: the wrinkles aligned at nearly 45° in the middle of the sheet, the fan shape transitions at the corners, and the small wrinkles aligned perpendicularly to the unloaded vertical edges. Our simulations capture all of these features. We note

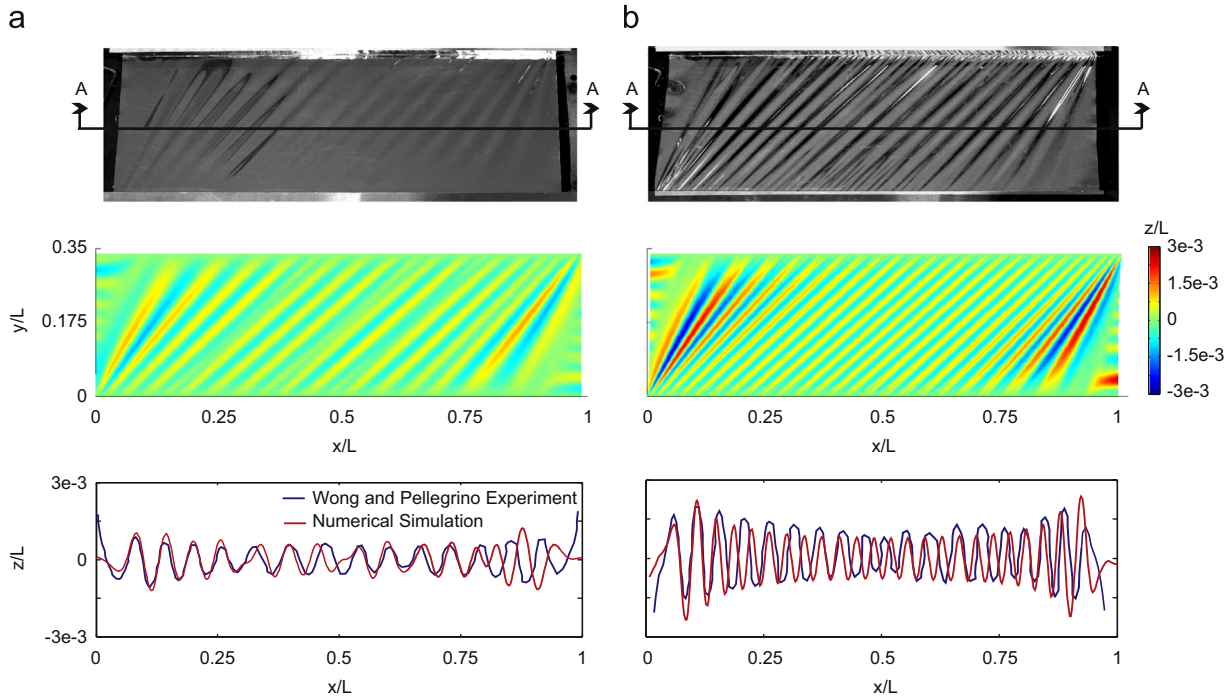

Fig. 6. Comparison of simulated sheet deformation with experimental images obtained by Wong and Pellegrino (2006a). Equilibrium positions shown for a top boundary displacement of 0.05 mm (a) and 3 mm (b). The first row shows the experimental images. The second row shows the corresponding simulated deformation. The third row compares out-of-plane deformation along a cross-section identified as 'A' in the experimental images.

that Wong and Pellegrino (2006c) performed a finite element buckling analysis for this problem. While their analysis captures the 45° wrinkles in the central region and the fan shape transitions, it appears to miss the features perpendicular to the unloaded edges (see Fig. 6 of Wong and Pellegrino, 2006c). From the cross-sectional plots shown in the third row of Fig. 6, we see quantitative agreement as well. In particular, the simulated data on the amplitude and wavelength of the wrinkles furnish remarkable agreement with the experimental data.

4.3. Extension of a rectangular Kapton sheet with an unloaded interior hole

This example is similar to that of Section 4.1 except that the sheet contains an interior hole which, together with the long edges, is free of traction and bending moment. The initial rectangular configuration of the sheet has dimensions 125 mm × 50 mm with thickness $h=0.01$ mm, and the central hole is initially circular with radius 15 mm. Positions and displacements are normalized using $L=125$ mm. The shorter edges are displaced apart by 10% of their original separation distance. We assume the material to be Kapton with the material properties given in Section 4.2.

Deformed equilibrium configurations are shown in Fig. 7a and b using the current thin-plate model and the tension-field theory membrane model, respectively. In both cases, we discretize the sheet using the same radial mesh of 40,000 nodes, biased such that more nodes are located near the central hole. The presence of the hole is predicted to have pronounced effects, including the redistribution of wrinkled regions and reorientation of the trajectories of the wrinkles. Also predicted are lightly stressed zones adjoining the extremities of the hole boundary at its major axes in the deformed configuration. The pattern shows remarkable agreement with the corresponding tension-field solution in which these zones are entirely slack, i.e. free of stress. The main difference between the present simulation and that delivered by tension-field theory is the detailed spatial resolution of the deformation of the wrinkled regions, as well as that of the 'slack' zones.

Fig. 8 depicts the distribution of maximum principal stretch, λ, in the sheet together with the predicted distributions of λ in regions adjoining the hole, as functions of distance from the hole center in orthogonal directions aligned with the edges of the initial rectangle. The corresponding tension-field theory solution is also shown, and indicates that the latter yields a remarkably accurate prediction of the stretch in wrinkled regions of the membrane. This agreement supports an earlier conjecture (Steigmann, 1990) to the effect that tension-field theory furnishes an accurate description of the tensile stress – and associated stretch – in wrinkled regions, despite its failure to model the detailed deformation pattern. That conjecture is based on the observation that tension-field theory yields the stress as the solution to a statically determinate system. Failure to accurately model the deformation is thus expected to have negligible effect on the predicted distribution of tensile stress transmitted along the trajectories of the wrinkle lines.

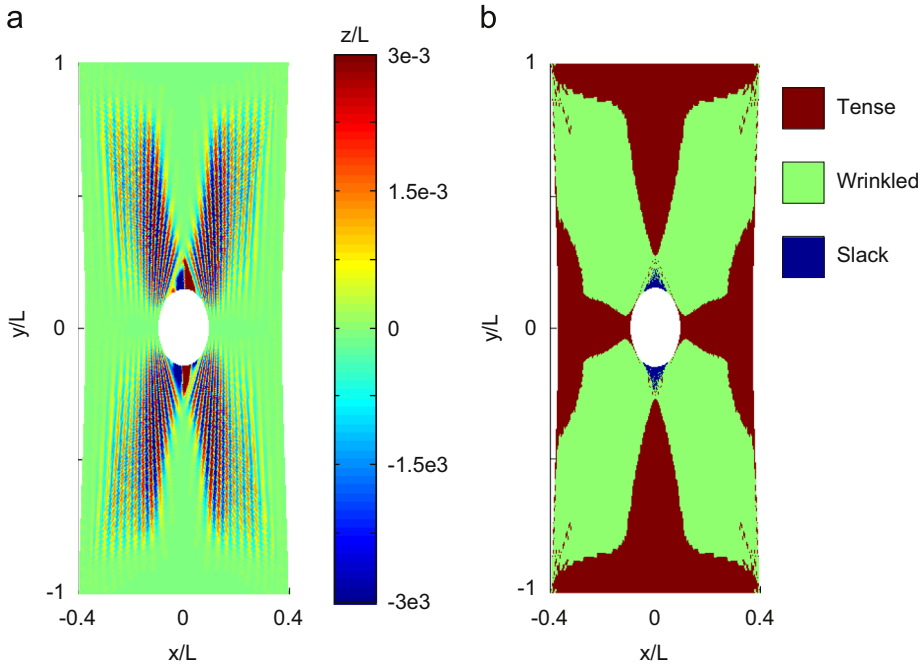

Fig. 7. Deformed equilibrium position of rectangular Kapton sheet with unloaded circular hole using the current thin-plate model (a) and tension-field theory (b).

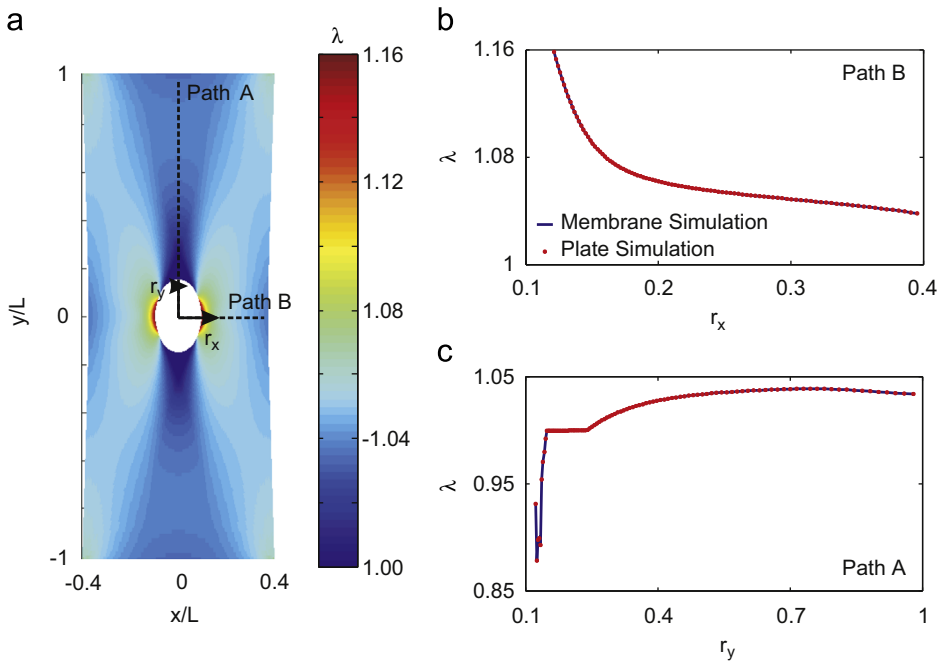

Fig. 8. Distribution of maximum principal stretch, λ, in sheet at equilibrium (a). Stretch values are compared between the current thin-plate model and the tension-field theory membrane model along two perpendicular paths r_x (Path B, (b)) and r_y (Path A, (c)) as measured in reference configuration coordinates.

4.4. Twist and pull-out of an annular sheet

This final example is inspired by the work of Haseganu and Steigmann (1994) on the numerical solution to problems in tension-field theory. A plane annular sheet is pinned at rigid concentric circular boundaries of radii 250 mm and 62.5 mm. The outer circle is fixed while the inner one is displaced out-of-plane by 125 mm and rotated through 90°. The positions and

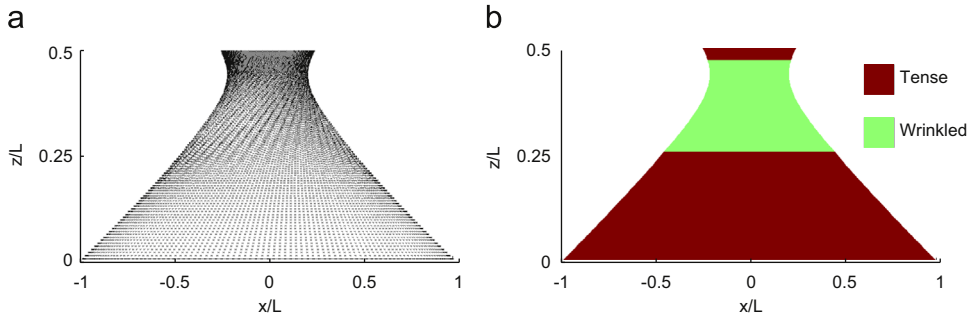

Fig. 9. Deformed equilibrium position of annular Kapton sheet with displaced central hole using the current thin-plate model (a) and the tension-field theory membrane model (b).

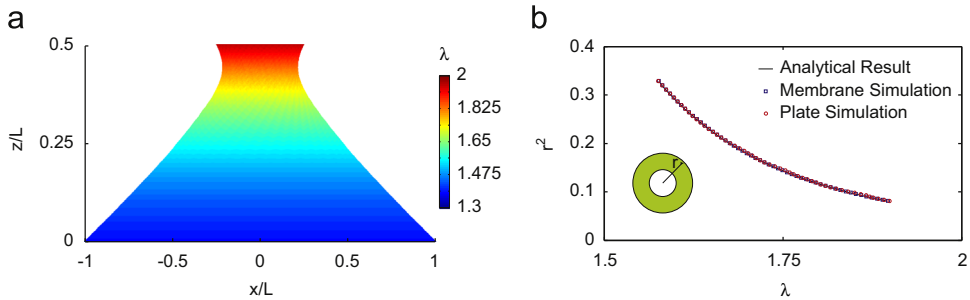

Fig. 10. Distribution of maximum principal stretch, λ, in sheet at equilibrium (a). Stretch values in the wrinkled region are compared among the current thin-plate model, the tension-field theory membrane model, and an analytical result along a radial trajectory, r, as measured in reference coordinates.

displacements are normalized using $L=250$ mm. The material is again taken to be Kapton. For results using the present model and those using tension-field theory, we use a center-hole-biased radial mesh with 20,000 nodes.

The solution yields the deformation and wrinkling pattern shown in Fig. 9. Again, there is very good agreement between the region predicted to be wrinkled using the tension-field theory, and the wrinkling observed in the current model. We draw attention to the narrow region near the inner boundary where wrinkling is suppressed. This prediction, which is common to simulations based on the present model and on tension-field theory (Haseganu and Steigmann, 1994), is corroborated by independent analysis (Roxburgh et al., 1994) and experiments on rubber sheets (Haseganu, 1994).

The tension-field theory solution exhibits a maximum principal stretch distribution which is axisymmetric in regions where wrinkling occurs (Haseganu and Steigmann, 1994). In this case an analytical result is known, based on an integral of the equations of tension-field theory (Steigmann, 1990). The distribution of the maximum principal stretch, derived from simulations based on the present model, is seen to be in excellent agreement with the analytical result derived from tension-field theory (Fig. 10). The present example thus provides further evidence in support of the foregoing conjecture regarding tension-field theory. Further work is needed, however, to assess the status of the conjecture in general boundary-value problems.

5. Concluding remarks

In this work we present a model for the finite bending and stretching of thin sheets derived from, and having optimal accuracy with respect to, three-dimensional nonlinear elasticity. We show this model to be tractable for numerical analysis by extending the method of dynamic relaxation to thin sheets exhibiting large deformations and wrinkling and solving several illustrative boundary-value equilibrium problems. The results obtained exhibit excellent agreement with available experimental data as well as with those obtained from the tension-field theory.

As stated previously, tension-field theory, which suppresses bending stiffness, is much more tractable than the alternatives. However, it does not model the detailed character of the deformation in wrinkled regions of the sheet (e.g. amplitude and wavelength). Our results indicate that it nevertheless furnishes a reliable estimate of the attendant stress distribution. In particular, the examples of Sections 4.3 and 4.4 show exceptional agreement between the current model and tension-field theory insofar as the maximum principal stretches are concerned, and also in the prediction of the locations where wrinkling occurs. Further, the current approach is applicable to a wide variety of problems without any a priori knowledge about the nature of the solution. In particular, it accommodates widespread wrinkling while incorporating the conventional limiting cases in which either membrane or bending behavior dominates.

Acknowledgments

MT and KB acknowledge the support of the Harvard Materials Research Science and Engineering Center under National Science Foundation Award DMR-0820484 and of startup funds from the School of Engineering and Applied Sciences, Harvard. DJS gratefully acknowledges the support of the Powley Fund for Ballistics Research.

References

Ben Amar, M., Dervaux, J., 2008. Morphogenesis of growing soft tissues. Phys. Rev. Lett. 101, 068101.
Cerda, E., Mahadevan, L., 2003. Geometry and physics of wrinkling. Phys. Rev. Lett. 90 (074302), 1–4.
Cerda, E., Ravi-Chandar, K., Mahadevan, L., 2002. Wrinkling of a stretched elastic sheet. Nature 419, 579.
Ciarlet, P., 2005. An Introduction to Differential Geometry with Applications to Elasticity. Springer, The Netherlands.
Ciarlet, P.G., Mardare, S., 2012. An intrinsic approach and a notion of polyconvexity for nonlinearly elastic plates. C. R. Acad. Sci. Paris 350 (I), 111–116.
Dacarogna, B., 1989. Direct Methods in the Calculus of Variations. Springer, Berlin.
Davidovitch, B., Schroll, R.D., Vella, D., Adda-Bedia, M., Cerda, E.A., 2011. Prototypical model for tensional wrinkling in thin sheets. Proc. Natl. Acad. Sci. U.S.A. 108 (45), 18227–18232.
Efimenko, K., Rackaitis, M., Manias, E., Vaziri, A., Mahadevan, L., Genzer, J., 2005. Nested self-similar wrinkling patterns in skins. Nat. Mater. 4, 293–297.
Friesecke, G., James, R., Muller, S., 2006. A hierarchy of plate models derived from nonlinear elasticity by gamma-convergence. Arch. Ration. Mech. Anal. 180, 183–236.
Haseganu, E., 1994. Analytical Investigation of Tension Fields in Lightweight Membrane Structures (Ph.D. thesis). University of Alberta, Edmonton, AB.
Haseganu, E., Steigmann, D., 1994. Analysis of partly wrinkled membranes by the method of dynamic relaxation. Comput. Mech. 14, 596–614.
Healey, T., Li, Q., Cheng, R.-B., 2013. Wrinkling behavior of highly stretched rectangular elastic films via parametric global bifurcation. J. Nonlinear Sci. http://dx.doi.org/10.1007/s00332-013-9168-3. Online.
Hilgers, M., Pipkin, A., 1992a. The graves condition for variational problems of arbitrary order. IMA J. Appl. Math. 48, 265–269.
Hilgers, M., Pipkin, A., 1992b. Elastic sheets with bending stiffness. Q. J. Mech. Appl. Math. 45, 57–75.
Hilgers, M., Pipkin, A., 1996. Bending energy of highly elastic membranes ii. Q. Appl. Math. 54, 307–316.
Kareklas, K., Nettle, D., Smulders, T., 2013. Water-induced finger wrinkles improve handling of wet objects. Biol. Lett. 9, 20120999.
Kezerashvili, R.Y. (Ed.), 2010. Proceedings of the Second International Symposium on Solar Sailing.
Kim, D., Ahn, J., Choi, W., Kim, H., Kim, T., Song, J., Huang, Y., Liu, Z., Lu, C., Rogers, J., 2008. Stretchable and foldable silicon integrated circuits. Science 320, 507–511.
Koiter, W., 1960. A consistent first approximation in the general theory of thin elastic shells. In: Koiter, W. (Ed.), Proceedings of the IUTAM Symposium on the Theory of Thin Elastic Shells, Delft. North-Holland, Amsterdam, pp. 12–33.
Koiter, W., 1966. On the nonlinear theory of thin elastic shells. Proc. K. Ned. Akad. Wet. B69, 1–54.
LeDret, H., Raoult, A., 1995. The nonlinear membrane model as a variational limit of nonlinear three-dimensional elasticity. J. Math. Pures Appl. 75, 551–580.
Nayyar, V., Ravi-Chandar, K., Huang, R., 2011. Stretch-induced stress pattern and wrinkles in hyperelastic thin sheets. Int. J. Solids Struct. 48, 3471–3483.
Pipkin, A., 1986. The relaxed energy density for isotropic membranes. IMA J. Appl. Math. 36, 85–99.
Puntel, E., Deseri, L., Fried, E., 2011. Wrinkling of a stretched thin sheet. J. Elasticity 105, 137–170.
Reissner, R., 1938. On tension field theory. Proc. V Int. Congr. Appl. Mech. 88.
Rezaiee-pajand, M., Kadkhodayan, M., Alamatian, J., Zhang, L., 2011. A new method of fictitious viscous damping determination for the dynamic relaxation method. Comput. Struct. 89, 783–794.
Rodriguez, J., Rio, G., Cadou, J., Troufflard, J., 2011. Numerical study of dynamic relaxation with kinetic damping applied to inflatable fabric structures with extensions for 3d solid element and non-linear behavior. Thin-Walled Struct. 49 (11), 1468–1474.
Roxburgh, D., Steigmann, D., Tait, R., 1994. Azimuthal shearing and transverse deflection of an annular elastic membrane. Int. J. Eng. Sci. 33, 27–43.
Schroll, R., Katifori, E., Davidovitch, B., 2011. Elastic building blocks for confined sheets. Phys. Rev. Lett. 106 (074301), 1–4.
Shugar, T., 1990. Automated Dynamic Relaxation Solution Algorithms for Compliant Systems. Technical Report. N-1812, Naval Civil Engineering Laboratory, Port Hueneme, CA.
Silling, S., 1988. Finite difference modelling of phase changes and localization in elasticity. Comput. Methods Appl. Mech. Eng. 70, 51–73.
Silling, S., 1989. Phase changes induced by deformation in isothermal elastic crystals. J. Mech. Phys. Solids 37, 293–316.
Sokolnikoff, I.S., 1951. Tensor Analysis: Theory and Applications. John Wiley and Sons, Inc., New York.
Steigmann, D.J., 1990. Tension-field theory. Proc. R. Soc. Lond. A 429, 141–173.
Steigmann, D.J., 2007. Thin-plate theory for large elastic deformations. Int. J. Non-linear Mech. 42, 233–240.
Steigmann, D.J., 2010. Applications of polyconvexity and strong ellipticity to nonlinear elasticity and elastic plate theory. In: Schroder, J., Neff, P. (Eds.), CISM Course on Applications of Poly-, Quasi-, and Rank-One Convexity in Applied Mechanics, vol. 516. . Springer, Wien and New York, pp. 265–299.
Steigmann, D.J., 2013. A well-posed finite-strain model for thin elastic sheets with bending stiffness. Math. Mech. Solids 13, 103–112.
Steigmann, D.J., Ogden, R.W., 1999. Elastic surface–substrate interactions. Proc. R. Soc. Lond. A 455, 437–474.
Taylor, M., Steigmann, D.J., 2009. Simulation of laminated thermoelastic membranes. J. Therm. Stresses 32, 448–476.
Topping, B.H.V., Khan, A.I., 1994. Parallel computation schemes for dynamic relaxation. Eng. Comput. 11 (6), 513–548.
Vandeparre, H., Gabriele, S., Brau, F., Gay, C., Parker, K.K., Damman, P., 2010. Hierarchical wrinkling patterns. Soft Matter 6, 5751–5756.
Vandeparre, H., Pineirua, M., Brau, F., Roman, B., Bico, J., Gay, C., Bao, W., Lau, C.N., Reis, P.M., Damman, P., 2011. Wrinkling hierarchy in constrained thin sheets from suspended graphene to curtains. Phys. Rev. Lett. 106 (224301), 1–4.
Vulpetti, G., Johnson, L., Matloff, G.L., 2008. Solar Sails: A Novel Approach to Interplanetary Travel. Copernicus Books, Springer Science+Business Media, New York, NY.
Wagner, H., 1929. Ebene blechwandtrhger mit sehr diinnem stegblech. Z. Flugtech. Motorluftschiffahrt 20 (8–12).
Wong, Y., Pellegrino, S., 2006a. Winkled membranes. Part 1: experiments. J. Mech. Mater. Struct. 1, 3–25.
Wong, Y., Pellegrino, S., 2006b. Winkled membranes. Part 2: analytical models. J. Mech. Mater. Struct. 1, 27–61.
Wong, Y., Pellegrino, S., 2006c. Winkled membranes. Part 3: numerical simulations. J. Mech. Mater. Struct. 1, 63–95.
Zheng, L., 2009. Wrinkling of Dielectric Elastomer Membranes (Ph.D. thesis). California Institute of Technology, Pasadena, CA.